Journal of Applied Fluid Mechanics, Vol. 15, No. 3, pp. 857-872, 2022.
Available online at www.jafmonline.net, ISSN 1735-3572, EISSN 1735-3645.
https://doi.org/10.47176/jafm.15.03.33352

Dynamics of Particle-Laden Wake Flow in a Karman Vortex Street Considering the Droplet-Vortex Interactions

J. Li[1], C. Wang[2], H. Ding[2†] and H. Sun[2]

[1] *College of Electronic Information and Automation, Civil Aviation University of China, Tianjin, 300300, China*
[2] *School of Electrical and Information Engineering, Tianjin University, Tianjin 300072, China*

†*Corresponding Author Email: hbding@tju.edu.cn*

(Received September 7, 2021; accepted January 3, 2022)

ABSTRACT

To investigate the dynamics of droplet-vortex interactions in particle-laden Karman vortex street flows, the simulations were carried out by using Euler-Lagrange approach, which was validated by the available experiments and numerical results. Then, the particle dispersion and the dimensionless frequency (Strouhal number) of the wake flow were analyzed to evaluate the particle-vortex interactions. The particle dispersion was statistically analyzed from both time and space dimensions and the different instantaneous dispersion patterns were explained by the relative slip velocity. Two independent scaling parameters, Stokes number St_L and particle-fluid mass loading ratio ϕ were revealed, and the particle mean square displacement and the Strouhal number were modelled by using these two scaling parameters, respectively. Finally, the characteristic lengths of the particle-laden wake flow were researched, and the Strouhal number physical model was developed based on the oscillating fishtail model. The results indicated that, firstly, St_L and ϕ, which constitute a dominant scaling group, can characterize the dynamics of droplet-vortex interactions in wake flow. Particles gradually separate from the vortex with the increase of St_L due to the centrifugal effect, and the vortex intensity and regularity get worse with the increase of ϕ, which further disperses the droplets for their momentum exchange with irregular vortex structures. Secondly, the length of the formation region and the width of the free shear layer diffuse are the two simultaneous characteristic lengths of the Strouhal number in oscillating wake. The proposed Strouhal number model gives a physical basis for the frequency determination, and the predicted errors are within ±1.5% error bands with mean absolute percentage error of 0.67%.

Keywords: Karman vortex street; Droplet dispersion; Unsteady; Vortex shedding; Strouhal number.

Nomenclature

English symbols

C_D, C_L, C_{pb}	drag, lift and base-pressure coefficients
d, d_p	diameter of the cylinder and the particle
$\mathbf{F}_p$	total force on the particles per unit volume
f_{VS}	vortex shedding frequency
H	width of the dead stream
h	width between the two vortex rows
L_f	length of the formation region
$L_{py}(x)$	particle dispersion width
l	distance of adjacent vortex in one vortex row
m^p	mass of a single particle
N^p	particle number inside ΔV_{cell}
p	pressure

Greek symbols

Δt	time step
δ_ω	width of the free shear layers diffuse
ϕ	particle-fluid mass loading ratio
λ_p	wave length of tracked particle trajectory
ν	kinematic viscosity
π	Pi constant
θ	oscillation angle of the fishtail
ρ_C	mass of particles per unit volume
ρ_f, ρ_p	fluid and particle density
τ_f	flow characteristic time
τ_p	particle aerodynamic response time
ω_v	oscillation angular frequency of the fishtail

p_b	pressure at the cylinder base (x = 0.5d, y =0)
p_0	inflow pressure
Re_f	fluid Reynolds number
Sr	Strouhal number
St	Stokes number defined in Burger *et al.* (2006)
St_L	macroscopic Stokes number
t	time
$\mathbf{U}$, $\mathbf{U}_p$	fluid and particle velocity vector
U, U_p	fluid and particle streamwise velocity
U_0	inflow fluid/superficial gas velocity
x, y, z	streamwise, radial and spanwise ordinate
$\overline{x_p^2(t)}$ $\overline{y_p^2(t)}$	particle mean square displacement at t
$\overline{y_p^2(x)}$	particle mean square displacement at x

Superscripts

∧	fluctuation amplitude
–	time-averaged value
*	non-dimensional variable

Subscripts

CFD	CFD results
exp	experimental results
pre	predicted results by the modelling

Abbreviations

CFL	Courant Friedriches Lewy number
MAPE	Mean Absolute Percentage Error
rRMSE	relative Root Mean Square Error

1. INTRODUCTION

In wake flows with the solid particle/liquid droplet laden, the particle-vortex interactions, play a crucial role in determining the structural characteristics (Yang *et al*. 2000), improving the metering accuracy of vortex flowmeter in wet steam/wet gas flow (Li *et al.* 2018), and estimating the performance of many industrial processes (Eaton and Fessler 1994), such as coal combustion systems, oil droplet fueled gas combustors, spray drying and cooling, pneumatic processing of food particles. The particle-laden wake flows are inherently complex involving multiple flow scales, boundary layer separation, wake vortex, and rapidly fluctuating pressure field (Burger *et al.* 2006). Besides, the dispersed phase and the vortex structures couple in a nonlinear manner, the vortex structures determine the particle dispersion, which in turn affects the local environment surrounding each particle/droplet and finally affects the dynamics of the two-phase systems (Park *et al.* 1996).

In past several decades, the particle-laden wake flow was investigated by many experiments (Bordás *et al.* 2013; Schmeyer *et al.* 2014) and simulations (Takahiko *et al.* 2009; Qiao *et al.* 2015), where the influence of large eddies on the particle dynamics is always focused on. For dilute particle-laden wake flow, an important scaling parameter, Stokes number (St) was introduced to predict the effect of organized vortex structures on the particle dispersion process (Crowe *et al.* 1985). Then different dispersion patterns at different orders of Stokes number were observed in experimental (Lazaro and Lasheras 2006) and numerical studies (Fan *et al.* 2004).

Obviously, the dispersed phase would also impact the vortex dynamics of carried phase, especially in the case of high particle-fluid concentration ratio (Crowe 1991). Fleckhaus *et al*. (1987) found that the particle-fluid mass loading ratio of 30% will cause significant change in flow properties. Burger *et al.* (2006) found that the lift coefficient would decrease with the increase of particle diameter. Yang *et al.* (1993) found that the presence of the particles can lower the vortex shedding frequency, which was also observed by Tang *et al.* (1969) and Aggarwal *et al.* (1996). It is noted that only the case of particle-laden flow with unladen flow was compared in Aggarwal *et al*. (1996), and the particle effects were analyzed using an implicit particle loading parameter A in Yang *et al*. (1993) without considering the viscosity of the fluid and the non-uniform particle distribution in the wake flow. To the best of the authors' knowledge, the systematic study on the dynamics of particle-laden wake flow, specifically the changing law of integral quantities (e.g. force and frequency characteristics) with the particle parameters were not reported, which is partly due to the lack of analysis on the scaling parameters which dominates the particle-vortex interactions. In addition, for the dimensionless frequency (Strouhal number) of the oscillation wakes, although several characteristic lengths were proposed to try to explain the physical basis for determination of the frequency (Gerrend 1966, Williamson and Brown 1998), however, there is still no universal formula developed, especially for the particle-laden wake flow involved complex particle-vortex interactions.

This study focuses on the dynamics of droplet-vortex interactions in wake flow. Two scaling parameters (i) Stokes number St_L and (ii) particle-fluid mass loading ratio ϕ, were acquired. The use of St_L and ϕ to sufficiently characterize the particle transport dynamics and the vortex dynamics was discussed by evaluating the particle dispersion and vortex shedding frequency, respectively. Then, the characteristic lengths of the particle-laden wake flow were revealed to study the physical basis for the determination of the frequency. Finally, the Strouhal number physical equation was developed based on the oscillating fishtail vortex shedding model.

2. NUMERICAL METHOD AND VALIDATION

2.1 Governing equations

To study the particle-vortex interactions, the following assumptions are made for the analysis in

particle-laden flow: (1) The flow is incompressible, laminar and Stokes flow; (2) The particles are spheres with diameters which are small enough compared to the scale of large-scale vortex structures; (3) The material density of the particles are much larger than that of the carrier fluid; (4) The particle-laden flow is dilute and the particle-particle interactions are ignored; (5) The particle-wall collisions are elastic.

For the continuous phase (gas), the continuity equation and the momentum equation are written as

$$\nabla \cdot \mathbf{U} = 0 \tag{1}$$

$$\frac{\mathrm{D}\mathbf{U}}{\mathrm{D}t} = -\frac{1}{\rho_f}\nabla p + \nu \nabla^2 \mathbf{U} - \frac{1}{\rho_f}\mathbf{F}_p \tag{2}$$

where $\mathbf{F}_p$ is the total force per unit volume exerted by the fluid onto the particles.

For the discrete phase, as mentioned in the assumptions, for heavy particles (density ratio ρ_p/ρ_f >>1, which is valid for gas-solid particle and gas-liquid droplet flows), the drag force is dominant and and the effect of other forces (pressure gradient force, lift force, virtual mass force etc.) is very small (about 1%) (Armenio and Fiorotto 2001). Therefore, only drag force is considered and the interphase force $\mathbf{F}_p$ in Eq. (2) is given by (Tomohiko and Eaton 2008)

$$\mathbf{F}_p = \frac{\rho_C}{\tau_p}\left(\mathbf{U} - \mathbf{U}_p\right) \tag{3}$$

where $\tau_p = (\rho_p/\rho_f)d_p^2/18\nu$ is particle aerodynamic response time; ρ_C (= $N^p \cdot m^p / \Delta V_{\mathrm{cell}}$) is the mass of particles per unit volume, N^p is the instantaneous number of particles inside a differential volume ΔV_{cell}.

Then, the momentum equations for gas and particle are

$$\frac{\mathrm{D}\mathbf{U}}{\mathrm{D}t} = -\frac{1}{\rho_f}\nabla p + \nu \nabla^2 \mathbf{U} - \frac{\rho_C}{\rho_f}\frac{\left(\mathbf{U} - \mathbf{U}_p\right)}{\tau_p} \tag{4}$$

$$\frac{\mathrm{d}\mathbf{U}_p}{\mathrm{d}t} = \frac{\mathbf{U} - \mathbf{U}_p}{\tau_p} \tag{5}$$

The Euler-Lagrange approach with Discrete Phase Model (DPM) was applied to simulate the particle-laden flow under the governing equations of Eq. (1), Eq. (4) and Eq. (5). The particle motion is solved by a Lagrangian method (Crowe *et al.* 1975) by tracking a large number of particles through the calculated unsteady, non-uniform flow field. The detailed flow chart of the simulation program is shown in Fig. 1.

2.2 Computational domain and numerical scheme

The calculations were performed using ANSYS® CFX on a two-dimension domain (shown in Fig. 2) since the instability producing the vortex street sheet is two-dimensional (Bloor 1964). The sufficient outflow length L_0 = 60d to avoid an effect of unphysical reflection from the outflow boundary (Posdziech and Grundmann 2007). The inflow and lateral length are also set as $L_i = L_b = 60d$ to avoid high Strouhal number artificially. To capture the gradients and flow profiles, the boundary layer needs to be well resolved, hence, the local mesh near the cylinder was refined to obtain a y^+ of about one. Boundary conditions were as follows, the non-dimensional inflow boundary was U^* =1, V^* = 0. The lateral boundary conditions were set as U^* =1, $V^* = \partial W/\partial y$ = 0, called free stream condition to eliminate the blockage effect (Posdziech and Grundmann 2007). No slip conditions were applied on the cylinder surface and symmetry boundary conditions in the spanwise direction, $\partial U/\partial z = \partial V/\partial z$ = 0. The outlet was set as 'opening' with pressure p = 0, which has good robustness and stability.

A second order backward Euler scheme was applied for the time-discretization. A high resolution scheme was applied for the advection discretization. The convergence criterion was set to 10^{-5}. A multigrid method was used to solve the discrete linear equations to enhance the convergence behavior, and in general, only two iterations for each time step were enough to satisfy the convergence criterion. In this study, the independent grid and time step were determined by monitoring drag and lift coefficient, base-pressure coefficient and Strouhal number at Re_f = 100, which are defined as

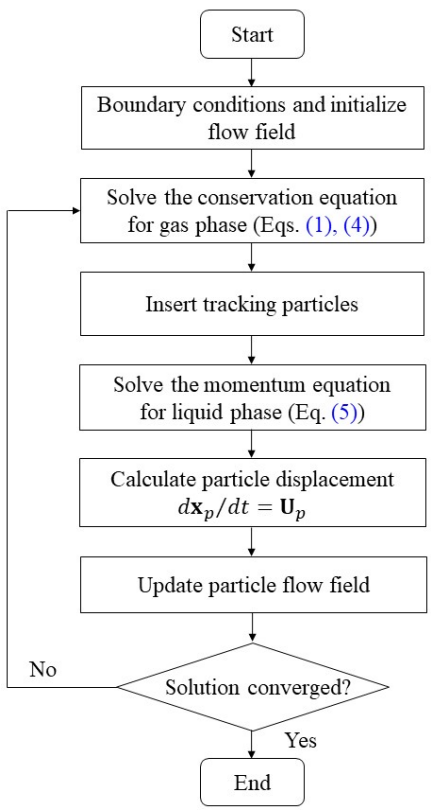

Fig. 1. Flow chart of the simulation program.

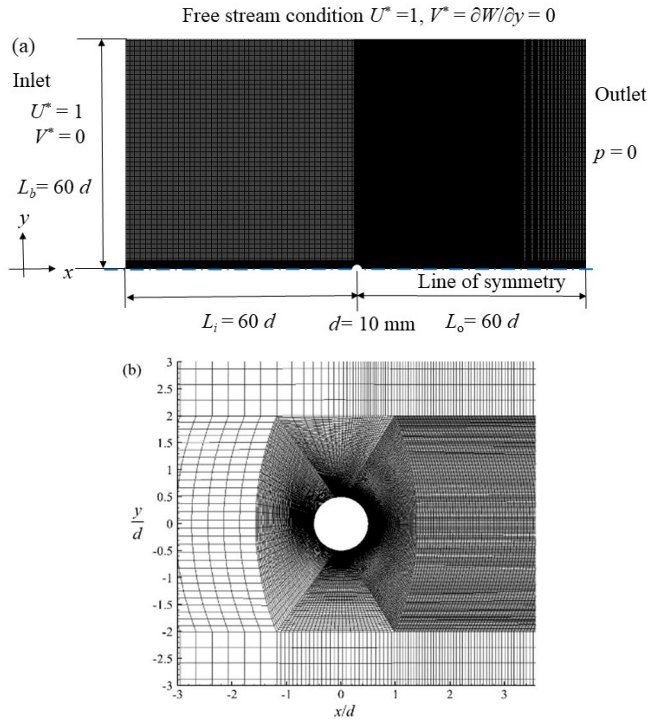

Fig. 2. Computational domain (a) one side of the domain and (b) local mesh near the cylinder.

Table 1 Numerical conditions and results for the grid and time step independent tests

Conditions			Numerical results			
Re_f = 100	Mesh nodes	Δt (s)	Sr	$\bar{C}_D$	$\hat{C}_L$	$-\bar{C}_{pb}$
Grid independence						
Mesh-1	1.0×10^5	0.002	0.1613	1.379	0.349	0.725
Mesh-2	2.9×10^5	0.002	0.1641	1.328	0.323	0.711
Mesh-3	4.8×10^5	0.002	0.1641	1.326	0.321	0.709
Mesh-4	6.1×10^5	0.002	0.1642	1.326	0.321	0.709
Time step independence						
Mesh-3	4.8×10^5	0.002	0.1641	1.326	0.321	0.709
Mesh-3	4.8×10^5	0.005	0.1639	1.326	0.319	0.708
Mesh-3	4.8×10^5	0.01	0.1624	1.325	0.318	0.706

$$C_D = \frac{Drag}{0.5\rho_f U_0^2 Ld},\quad C_L = \frac{Lift}{0.5\rho_f U_0^2 Ld},$$
$$C_{pb} = \frac{p_b - p_0}{0.5\rho_f U_0^2},\qquad Sr = \frac{f_{VS} d}{U_0} \tag{6}$$

The numerical conditions and results are listed in Table 1, where the superscript, –, denotes the time-averaged value, ^, denotes the fluctuation amplitude.

The time average stream-wise velocity profile at the wake centerline for various mesh sizes, time steps and particle numbers is shown in Fig. 3. Four meshes were firstly tested with a time step of 0.002s and the medium resolution with 4.8×10^5 nodes (Mesh-3) is selected as the final mesh. Then the time step is slightly increased to save the computational resources. From Table 1 and Fig. 3 a), the time step Δt = 0.002s is used to ensure the solution accuracy, which makes the average Courant Friedriches Lewy number (CFL=$U\Delta t/\Delta x$) (Dougherty *et al.* 2006) is about one.

For the discrete phase, the particles were injected in the projection area of the cylinder's cross-section at the same velocity with gas phase, similar to Burger *et al.* (2006). To better track particle trajectory, particles were injected every gas iteration with Δt = 0.002s, in general 4~5 iterations were needed for a time step. Particles were fully coupled with gas phase and the particle source change target for convergence was set to be 0.01. From Fig. 3(b), with different particle number rates laden, the results show no significant changes. In this study, the number rate of 10000/s is set for all the particle-laden flow.

2.3 Code validation

To validate the numerical methods for fluid flow, the results are compared with literatures in Fig. 4. An excellent agreement is found for Strouhal

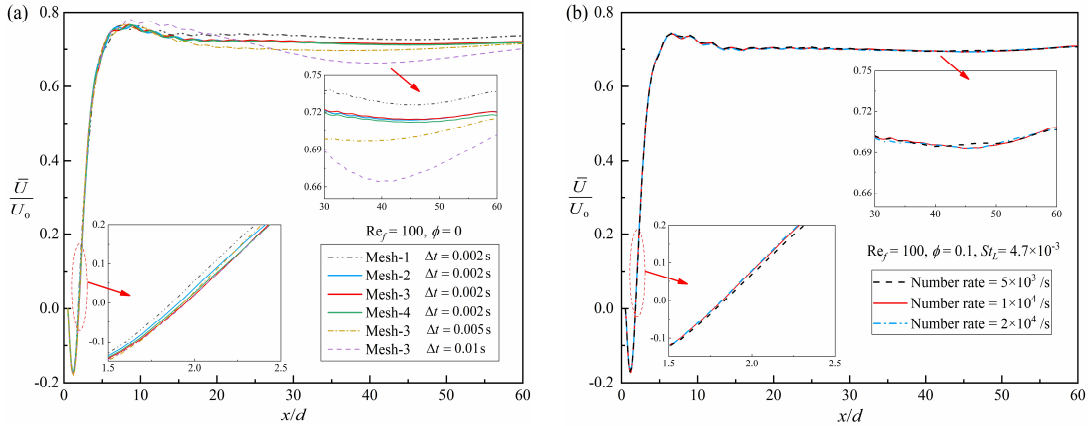

Fig. 3. Time-averaged stream-wise velocity profile at the wake centerline for (a) various meshes, time steps in gas flow and (b) various particle number rates in particle-laden flow.

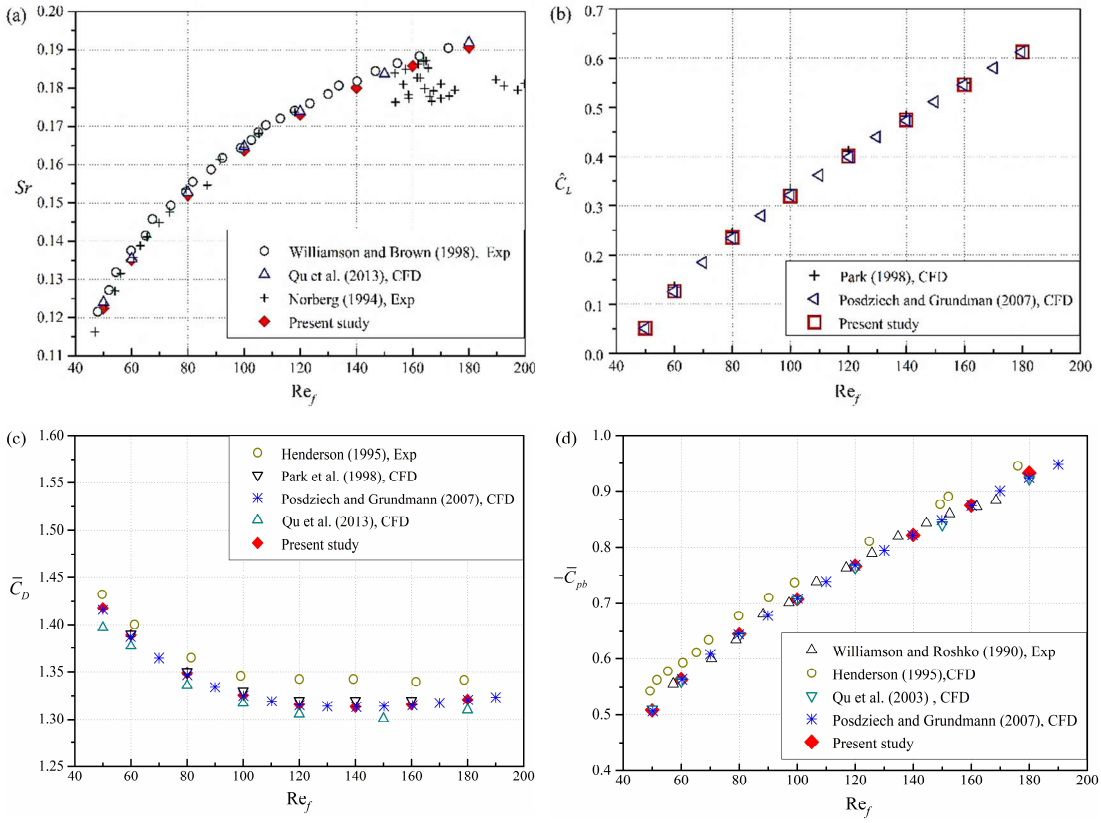

Fig. 4. Coefficients as a function of Reynolds number
(a) Strouhal number ; (b) Fluctuation amplitude of the lift coefficient; (c) Time-average drag coefficient; (d) Time-average base pressure coefficient.

number (Fig. 4 a) and lift coefficient (Fig. 4 b). The discontinuity in the experiments in Norberg (1994) is because the laminar vortex shedding could not be maintained for Re_f>165, which is most likely due to the influence of the end plates, as discussed in Williamson (1995). The drag coefficient (Fig. 4 c) and base-pressure coefficient (Fig. 4 d) show a large scatter, which may due to the limited experimental conditions and the deviation of numerical methods, as discussed in Qu *et al*. (2013). It should be noted that present results are perfectly in agreement with that in Posdziech and Grundmann (2007).

To validate the numerical method for particle tracking, the instantaneous particle distributions in Karman vortex street with different particle diameters are shown in Fig. 5 and compared with the results in Burger *et al*. (2006), which shows good agreement. The parameter h/l of the present study is 0.262, which is very close to 0.265 reported in Burger *et al*. (2006). The quantitative comparison of lift and drag coefficients is shown in Fig. 6, where the Stokes number is defined as $St = \tau_p \cdot f_{VS}$, and the cut-off Stokes number $St_{\text{cut-off}} = 1/2\pi$. From Fig. 6 a),

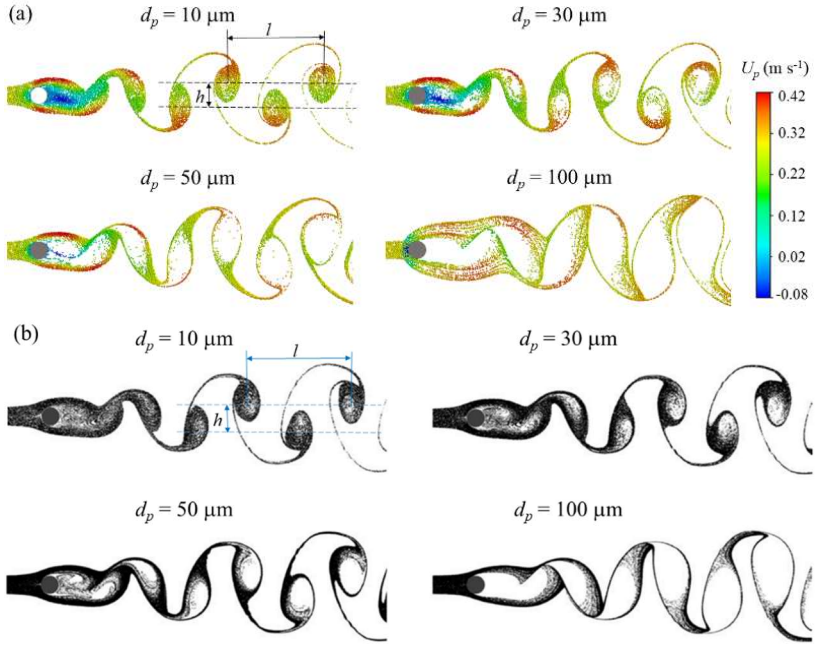

Fig. 5. Instantaneous particle distribution in Karman vortex street (Re$_f$ =100, *d* = 7.5 mm, one-way coupled) (a) present results (b) Results of Burger *et al*. (2006).

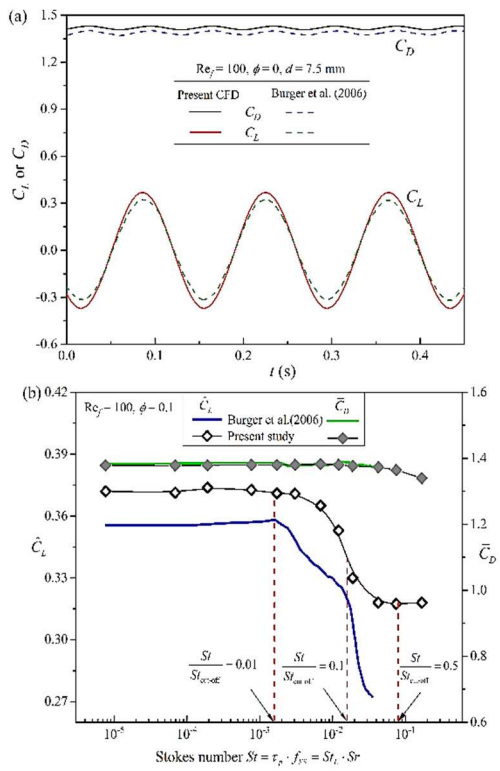

Fig. 6. Comparison with the lift and drag coefficients in Burger *et al*. (2006) (a) time series in gas flow (b) statistical results in particle-laden flow (two-way coupled).

the results are very close; from Fig. 6 b), the change law with Stokes number is basically the same with the results in Burger *et al*. (2006). The discrepancies may result from the different computational domain sizes and the different boundary conditions (Posdziech and Grundmann 2007). Through the above comparisons, the numerical method is validated.

3. Particle Dispersion in Karman Vortex Street

To obtain the scaling parameters for particle-laden flow, Eq.(4) is nondimensionalized as

$$\frac{\mathrm{D}\mathbf{U}^*}{\mathrm{D}t^*} = -\nabla p^* + \frac{1}{\mathrm{Re}_f}\nabla^2\mathbf{U}^* - \frac{\phi}{St_L}\mathbf{w}^* \tag{7}$$

where superscript,*, denotes a nondimensional variable, $\mathbf{U}^* = \mathbf{U}/U_0, t^* = tU_0/d, p^* = (p - p_0)/\rho_f U_0^2$, $\mathbf{w}^* = (\mathbf{U} - \mathbf{U}_p)/U_0$. Three nondimensional parameters, the gas Reynolds number $\mathrm{Re}_f = U_0 d/\nu$, the particle-fluid mass loading ratio $\phi = \rho_C/\rho_f = m_p/m_f$, and the macroscopic Stokes number $St_L = \tau_p/\tau_f = (\rho_p/\rho_g) d_p^2 U_0/18\nu d$ have been introduced here, where the flow characteristic time $\tau_f = d/U_0$.

Equation (7) reveals that, in addition to fluid Reynolds number Re$_f$, the scaling parameters related to the particle include (i) the macroscopic Stokes number St_L and (ii) particle-fluid mass loading ratio ϕ. Then to investigate the complex droplet-vortex interactions, CFD simulations were conducted at laminar flow condition (48 < Re$_f$ <180) according to above scaling parameter analysis.

3.1 Instantaneous particle dispersion patterns

To study the effects of St_L and ϕ on the particle response and dispersion in the vortex structures, the

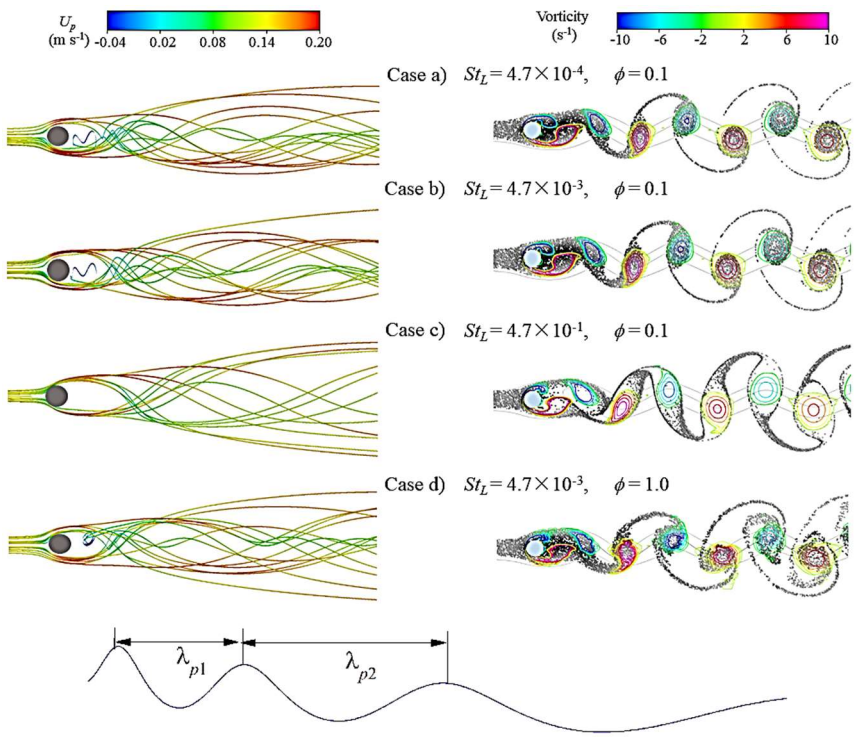

Fig. 7. Tracked particle trajectory (left) and phase-locked transient particle dispersion (right).

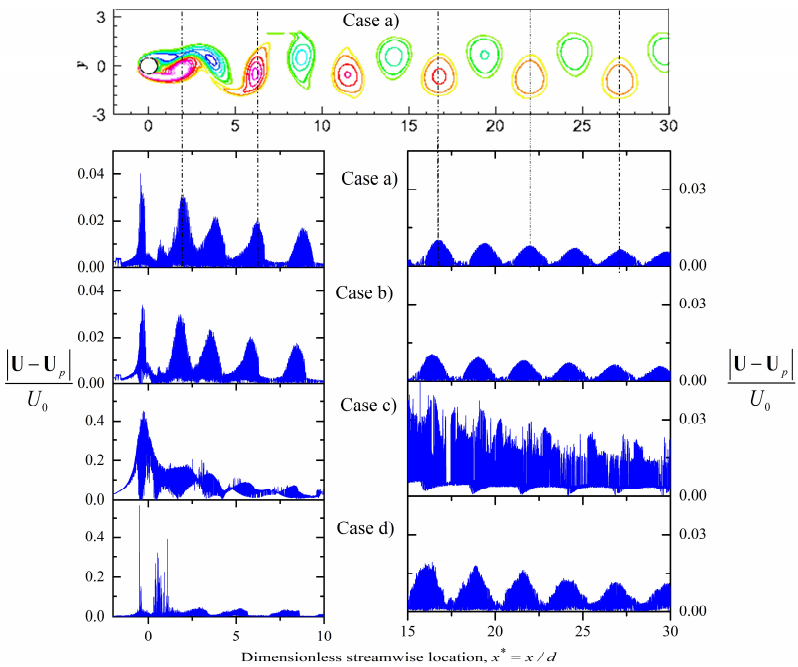

Fig. 8. Phase-locked droplet relative slip velocity along axial direction.

results of four typical cases listed in Table 2 are analyzed in detail.

The tracked particle trajectory, the phase-locked particle dispersion with vorticity contour (color map) and the gas streamlines (lines) are shown in Fig. 7, where the snapshots were taken from the transient results corresponding to the maximum separation angle to phase-lock the wake flows. To compare the particle motion quantitatively, the wave length of the particle trajectory λ_{p1} and λ_{p2} are listed in Table 2, denoted as mean ± SD (Standard Deviation). To understand the particle behavior, the phase-locked relative slip velocities along axial direction are shown in Fig. 8.

From Fig. 8, we can see that the peak of slip velocity appear at the vortex center, which indicates that

Table 2. Numerical parameters and the wave length of particle trajectory calculated from Fig. 7

Case No.	St_L	ϕ	d_p (μm)	ρ_p (kg/m^3)	λ_{p1}/d	λ_{p2}/d
Case a)	4.7×10^{-4}	0.1	10	100	13.824 ± 0.582	24.162 ± 1.595
Case b)	4.7×10^{-3}	0.1	10	997	13.921 ± 0.792	23.835 ± 2.019
Case c)	4.7×10^{-1}	0.1	100	997	18.515 ± 3.099	36.333 ± 6.625
Case d)	4.7×10^{-3}	1.0	10	997	14.594 ± 1.233	27.794 ± 3.592

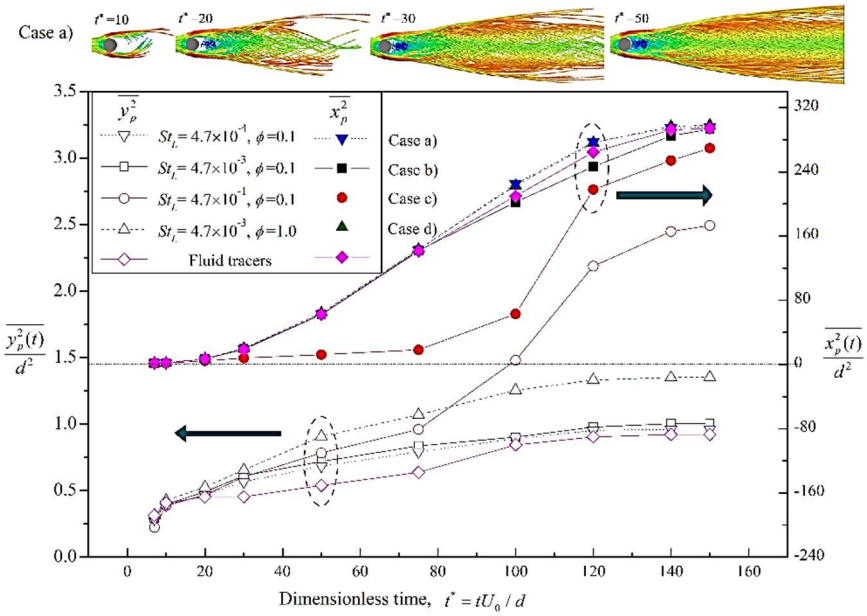

Fig. 9. Lagrangian measurements of the particle dispersion with dimensionless time *t.**

velocity slip is more likely to occur at the center of vortex. For Case a) and Case b) with small values of ϕ and St_L, the particles distribution can exactly reproduce the vortex. (Fig. 7), indicating a good particle following performance, meanwhile, the wave length of particle trajectory λ_{p1} and λ_{p2} have no obvious change (Table 2). For Case c) with large St_L, the vortex street could not be reproduced by the particles distribution (Fig. 7), less particles could reach the vortex core region. The velocity slip magnitude of Case c) is about one order larger than Case a) and Case b), indicating a strong particle accumulation effect (Fig. 8). As a result, it's more difficult for the larger particles to oscillate in gas flow, which is also reflected by the larger λ_p in Table 2. For Case d) with larger ϕ, the particle distribution is messy both around the vortex and on the junction of two vortexes (Fig. 7), and compared with Case b) with the same Stokes number, λ_p in Table 2 as well as the slip velocity in Fig. 8 increase, which both indicates a strong momentum exchange for droplets with the irregular vortex structures due to the droplet-vortex interactions.

To sum up, the parameter Stokes number mainly influence the droplet dispersion and the response to the vortex structures, while the parameter mass loading ratio mainly affects the regularity of the shedding vortex, then further affect the dispersion through the momentum exchange with the droplets.

3.2 Eulerian and Lagrangian measurements of particle dispersion

To analyze the particle dispersion characteristics in Karman vortex street, both Eulerian and Lagrangian measurements were carried out. The Lagrangian measurements of particle dispersion with dimensionless time t^* are shown in Fig. 9, where the particle mean square displacement in *x*-direction and *y*-direction are

$$\overline{x_p^2(t)} = \frac{1}{N(t)}\sum_{j=1}^{N(t)}\left[x_{pj}(t) - x_m(t)\right]^2,\ x_m(t) = \frac{1}{N(t)}\sum_{j=1}^{N(t)} x_{pj}(t) \tag{8}$$

$$\overline{y_p^2(t)} = \frac{1}{N(t)}\sum_{j=1}^{N(t)}\left[y_{pj}(t) - y_m(t)\right]^2,\ y_m(t) = \frac{1}{N(t)}\sum_{j=1}^{N(t)} y_{pj}(t) \tag{9}$$

where $x_{pj}(t)$ is the streamwise ordinate from $x = 0$, $y_{pj}(t)$ is the lateral ordinate from the center of the wake $y = 0$, $N(t)$ is the number of the particle introduced into the flow field for a given time *t*. The measurements were calculated by tracking 2000 particles. The dispersion of Case a) with time is given as an example.

As time goes by, $\overline{x_p^2(t)}$ and $\overline{y_p^2(t)}$ both increase first and then tend to be constant. In *x*-direction, $\overline{x_p^2(t)}$ increases slowly on larger Stokes number condition (Case c), especially in initial times, which is mainly

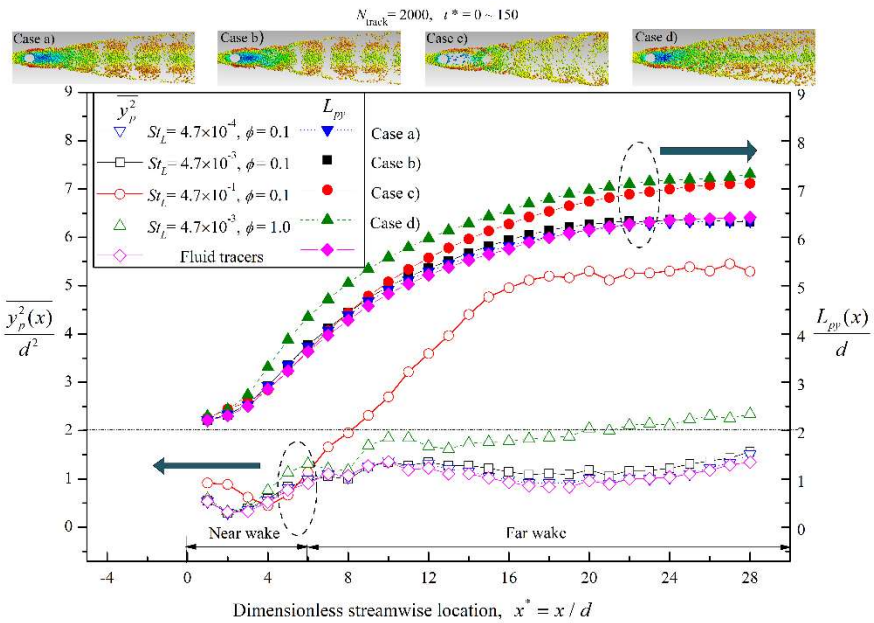

Fig. 10. Particle dispersion at different downstream locations.

due to the slow particles response to the oscillating gas flow. In y-direction, $\overline{y_p^2(t)}$ increases with Stokes number St_L, which is due to their different particle responses shown in Fig. 9. $\overline{y_p^2(t)}$ also increases with mass loading ratio ϕ, which is mainly subjected to the essay particle distribution around the irregular vortex structures (Case d in Fig. 7).

It is shown in Fig. 9 that the particle dispersion pattern is basically stable on $t^* = 150$. To study the particle spatial distribution in the wake flow, the particle dispersion at different downstream locations is shown in Fig. 10, where the particle dispersion width $L_{py}(x)$ and particle mean square displacement $\overline{y_p^2(x)}$ (Yang *et al.* 2000) are calculated during $t^* = 0\sim 150$

$$L_{py}(x) = y_p(x)_{\max} - y_p(x)_{\min} \tag{10}$$

$$\overline{y_p^2(x)} = \frac{\sum_{i=1}^{M(x)} n_i(x)\left[y_{pi}(x) - \overline{y_{pm}(x)}\right])^2}{\sum_{i=1}^{M(x)} n_i(x)}, \qquad \overline{y_{pm}(x)} = \frac{\sum_{i=1}^{M(x)} n_i(x) y_{pi}(x)}{\sum_{i=1}^{M(x)} n_i(x)} \tag{11}$$

where $n_i(x)$ is the particle number passing through the ith sampling bin, $M(x)$ is the bin number a t a given downstream x, $y_{pi}(x)$ is the lateral ordinate of the ith bin. The measurements were calculated by tracking 2000 particles and more than 1 million particle locations are recorded totally.

For convenience, the wake is divided into the near wake ($0 < x^* < 6$) and the far wake ($x^* > 6$) artificially. For the particle dispersion width L_{py}, the effect of Stokes number St_L becomes outstanding gradually in the far wake (Case c) due to the centrifugal effect. The case with larger mass loading ratio (Case d) shows larger dispersion width both in the near wake and far wake, which is also due to the essay particle distribution around the irregular vortex structures (Fig. 7). For $\overline{y_p^2(x)}$ in the far wake, both larger Stokes number and larger mass loading ratio leads to enhanced particle dispersity, which is consistent with Fig. 9. In the near wake, $\overline{y_p^2(x)}$ decreases first and then increases, which is due to the existence of formation region (for detail in Section 4.2) where back flow occurs both for gas flow and particles.

3.3 Statistical analysis and modelling of particle dispersion

To investigate the dispersion on different droplet-laden conditions, the statistical analysis and modelling for particle mean square displacement were conducted. From the results in Fig. 9 and Fig. 10, the particle dispersion pattern at $x^* = 24$ on $t^* = 150$ is basically stable, thus, the particle mean square displacement $\overline{y_p^2}$ is calculated at $x^* = 24$ by tracking 2000 particles during $t^* = 0\sim 150$. The particle mean square displacement $\overline{y_p^2}$ as a function of Stokes number and mass loading ratio is plotted in Fig. 11. It is shown that $\overline{y_p^2}$ is positively related with Stokes number and mass loading ratio, and the larger the Stokes number is, the greater the particle disperser tends to be, which agrees with the results in Section 3.2.

Based on the above analysis, the particle mean square displacement is modelled by the semi-empirical equation

$$\frac{\overline{y_p^2}}{d^2} = a_0 + a_1 St_L + a_2\phi + a_3 St_L^2 + a_4 St_L\phi \tag{12}$$

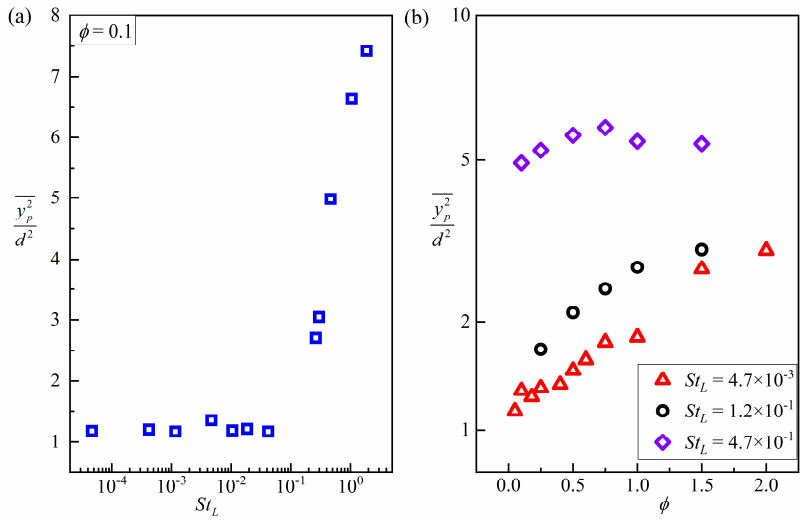

Fig. 11. Particle mean square displacement as a function of (a) Stokes number (b) mass loading ratio.

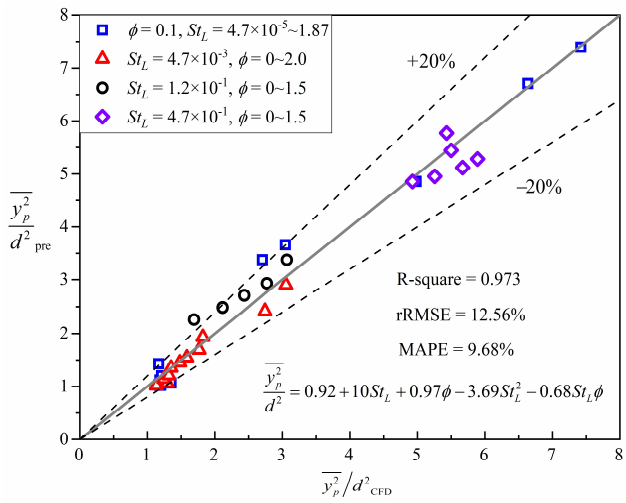

Fig. 12. Comparison between the actual and predicted particle mean square displacement.

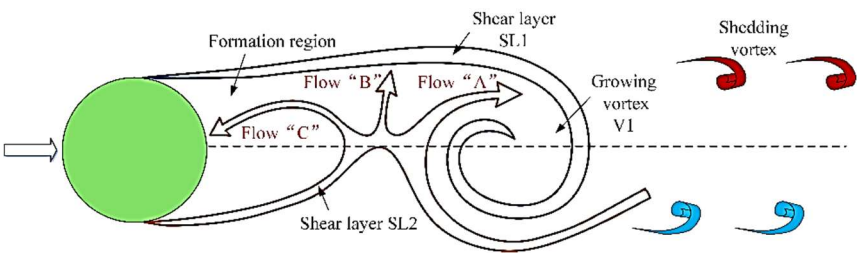

Fig. 13. Diagram of the vortex street and roll-up of the shear layers.

where $a_0 = 0.92$, $a_1 = 10.0$, $a_2 = 0.97$, $a_3 = -3.69$, $a_4 = -0.68$. The predicted results of Eq. (12) is plotted in Fig. 12, 85.3% of the points located within ±20% error bands, the coefficient of determination R-square is 0.973, the relative root mean square error (rRMSE) is 12.56%, and the mean absolute percentage error (MAPE) is 9.68%.

From the above analysis, it indicated that Stokes number St_L and mass loading ratio ϕ can be as dominant scaling group which can be used to characteristic particle dispersion dynamics in Karman vortex street flows.

4. FREQUENCY CHARACTERISTICS IN PARTICLE-LADEN WAKE FLOW

The vortex street formation based on shear layer theory was described in Roshko (1954), Gerrend (1966), which involves three streams (Fig. 13). Flow "A" entrained into the growing vortex V1 generated

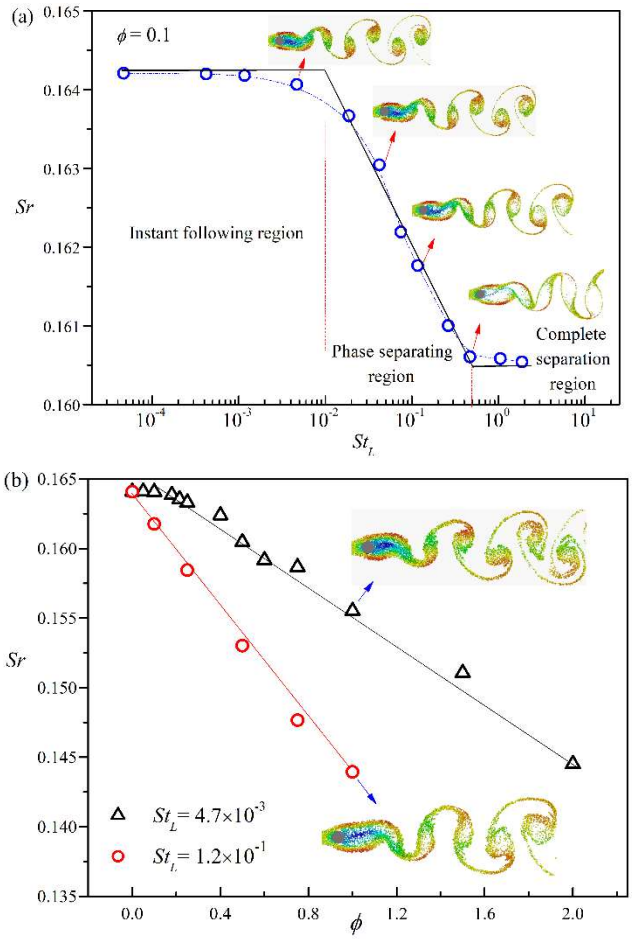

Fig. 14. Strouhal number as a function of (a) Stokes number and (b) mass loading ratio.

from the opposite shear layer SL1; Flow "B" entrained by the shear layer SL2; Flow "C" (reverse flow) directed back into the formation region and generating a new vortex. When the growing vortex V1 becomes strong enough to draw SL2 across the wake, V1 sheds from the bluff body and developed to be mature shedding vortex in the wake flow.

4.1 The effect of St_L and ϕ on Strouhal number

The frequency characteristic is very important for the vortex dynamics of wake flow in Karman vortex street as well as the droplet-vortex interactions. The non-dimensional frequency, Strouhal number is plotted against St_L and ϕ in Fig. 14, where $Sr = f_{VS} d/U_0$, U_0 is the superficial gas velocity.

Strouhal number decreases with the laden of particles, which agrees with the simulation results in Tang *et al.* (1969) as well as the analytical results in Yang *et al*. (1993). From Fig. 14 a), with the increase of Stokes number, Sr first decreases then tend to be constant. Three different regions can be observed. In the instant following region ($St_L < 10^{-2}$) and complete separation region ($St_L \geq 0.5$), Sr is almost unchanged; in the phase separation region ($10^{-2} \leqslant St_L < 0.5$), Sr decreased constantly. From Fig. 14 b), Strouhal number decreases with mass loading ratio, yet the decrease rate for moderate Stokes number is larger than of small Stokes number, which agrees with Fig. 14 a).

Based on the law in Fig. 14 and the parametric analysis results in Section 3, the Strouhal number is modelled by the following semi-empirical equation

$$Sr = Sr_0(1 - k_1 St_L^{\alpha}\phi) \tag{13}$$

where Sr_0 is the Strouhal number in single-phase gas flow, k_1 is constant coefficient, and α is power exponent. In this study, $Sr_0 = 0.1641$, $k_1 = 0.2$, $\alpha = 0.2456$. The predicted results by Eq. (13) is plotted in Fig. 15, the percentage errors are within $\pm 2.0\%$ error bands, the coefficient of determination R-square is 0.978, the relative root mean square error (rRMSE) is 0.67%, and the mean absolute percentage error (MAPE) is 0.52%.

From the above analysis, it is concluded that Stokes number St_L and mass loading ratio ϕ can be as dominant scaling group of the wake vortex dynamics in the particle-laden wake flow, in other words, they can characterize the dynamics of droplet-vortex interactions in Karman vortex street flows.

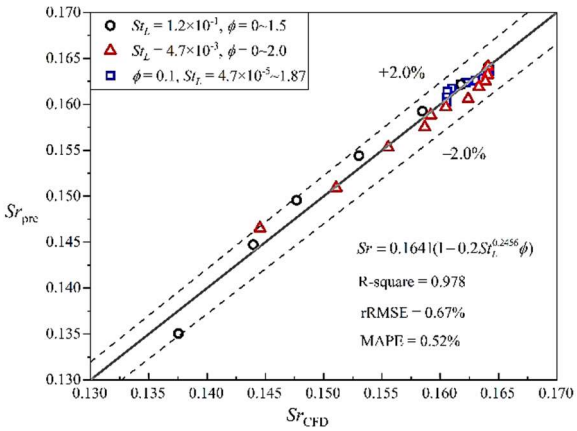

Fig. 15. Comparison between the actual and predicted Strouhal number by Eq. (13).

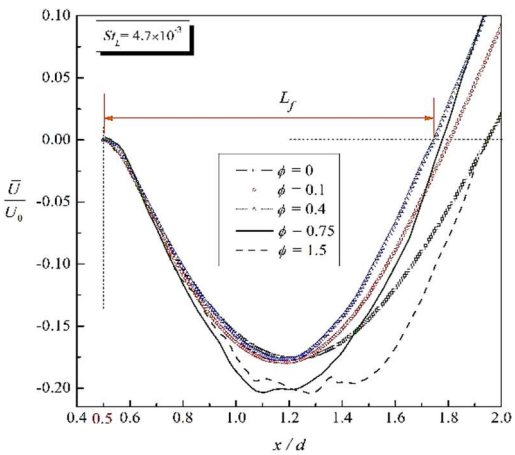

Fig. 16. Time-averaged stream-wise velocity profile at the wake centerline.

4.2 Characteristic lengths of the wake flow Journals

In Section 4.1, the Strouhal number equation is developed with the scaling parameters Stokes number and mass loading ratio. However, the mechanism of these two scaling parameters on the vortex shedding frequency is still unrevealed. To explain the physical basis for the determination of frequency characteristic, several different characteristic lengths were proposed, including the wake width by Roshko (1954), the length of formation region and the width of free shear layers diffuse by Gerrend (1966), and the total wake momentum thickness by Goldburg *et al.* (1965). To investigate the mechanism of particle effects on the vortex shedding frequency, the characteristic lengths would be analyzed.

From the shear layer theory in Fig. 13, it is well accepted that the scale of the formation region is a basic mechanism determining the frequency of vortex shedding (Gerrend 1966). In this study, the length of formation region (short as formation length) L_f was determined as the length from the rear surface of the cylinder ($x = 0.5d$, $y = 0$) to the second point of vanishing the average velocity $\bar{U}$, from

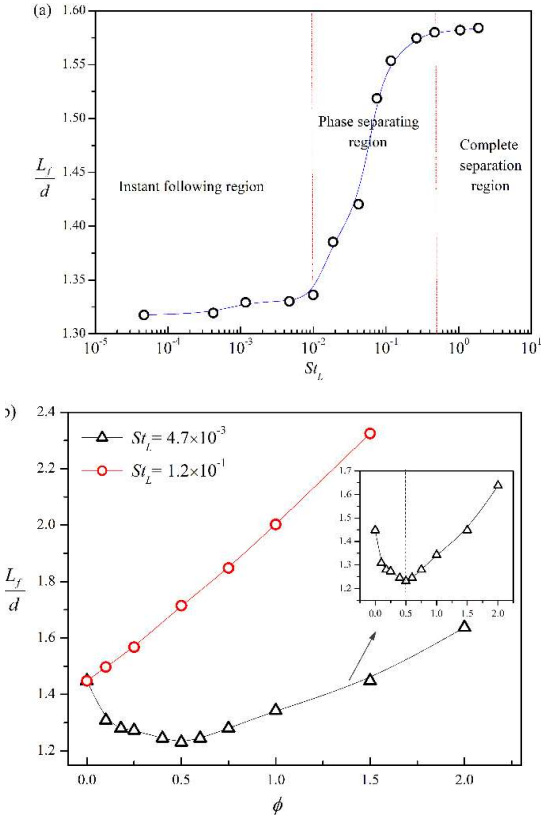

Fig. 17. Formation length as a function of (a) Stokes number and (b) mass loading ratio.

negative to positive values (Qu *et al.* 2013), as shown in in Fig. 16, where the velocity profile was taken from the time-averaged flow field at the wake centerline ($y = 0$).

For the particle-laden wake flow, the formation length L_f is plotted against St_L and ϕ in Fig. 17. From Fig. 17 a), L_f presents an asymptotic trend, and only particles with moderate Stokes number will cause obvious increase for formation length L_f. The three different regions (instant following region, phase separation region and complete separation region) in Fig. 14 a) can also be observed with the increase of Stokes number. From Fig. 17 b), L_f presents different trend with mass loading ratio, it increases constantly on moderate Stokes number condition, yet decreases slightly first and then increase on small Stokes number condition.

In addition to formation length, the width of free shear layer diffuse (short as shear layer thickness) is suggested to be another major effect for vortex shedding frequency (Gerrend 1966). In this study, the shear layer thickness δ_ω is taken as the diffusion length at the end of the formation region, defined as (Monkewitz and Nguyen 1987)

$$\delta_\omega = \frac{U_{y=\infty} - U_{y=0}}{(dU/dy)_{\max}} \tag{14}$$

where $U_{y=\infty}$ and $U_{y=0}$ denote the streamwise velocity at the infinity and at the wake centerline $y =$

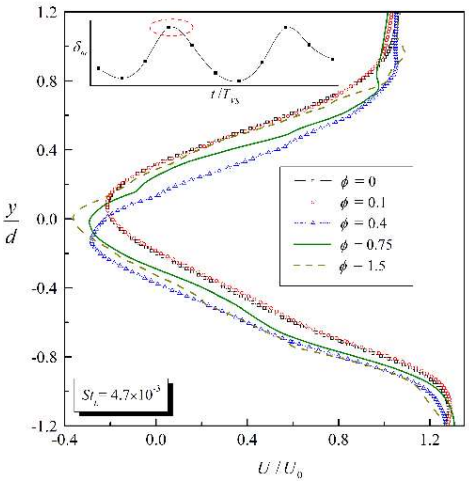

Fig. 18. **Velocity profile at the end of formation region**.

0, respectively. The velocity profile at the end of formation region is shown in Fig. 18, where snapshots were taken from the transient results corresponding to the maximum shear layer thickness.

Since the shear layer thickness δ_ω changes periodically during the vortex shedding process, in this study, the time-averaged shear layer thickness $\overline{\delta}_\omega$ is extracted and plotted against St_L and ϕ in Fig. 19, where the error bars denote the standard deviation in a vortex shedding period. From Fig. 19 a), $\overline{\delta}_\omega$ presents an asymptotic trend with Stokes number similar to the law of L_f in Fig. 17 a). From Fig. 19 b), $\overline{\delta}_\omega$ decreases constantly with mass loading ratio in small Stokes number case. On moderate Stokes number condition, $\overline{\delta}_\omega$ decreases first then tends to be a constant.

As discussed in Gerrard (1966), the frequency of vortex shedding is closely related with the balance between entrainment into the shear layers and the replenishment by reversed flow. The length of the formation region and the width of free shear layer diffuse could characterize this balance process described in Fig. 13. They both affects the shedding frequency by influencing the vortex growing and shedding, leading to the change of frequency characteristics in particle-laden wake flow.

4.3 Strouhal number physical model

In Section 4.1, the Strouhal number mathematic model is established with the external scaling parameters Stokes number and mass loading ratio. To study the physical basis for the determination of the frequency characteristics, the physical equation will be developed with the two characteristic lengths proposed in Section 4.2.

The variations of the formation length and the shear layer thickness with Strouhal number are plotted in Fig. 20, for convenient, the time-averaged shear layer thickness $\overline{\delta}_\omega$ is abbreviated as δ_ω in the rest of

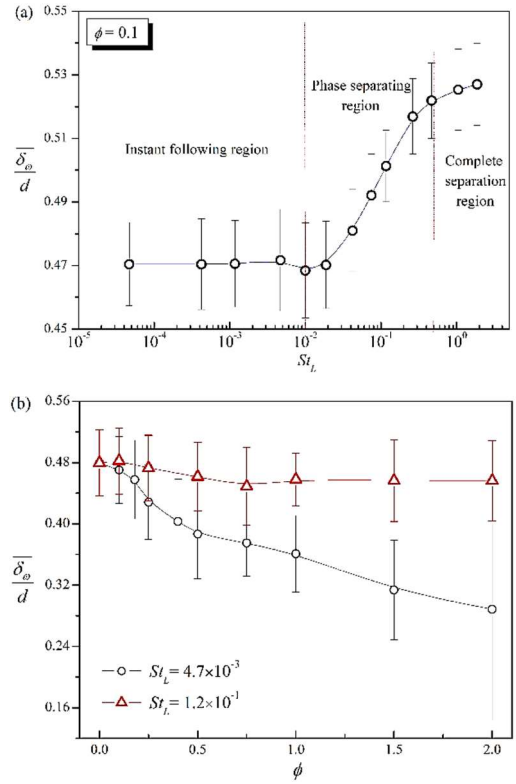

Fig. 19. **Shear layer thickness as a function of (a) Stokes number and (b) mass loading ratio**.

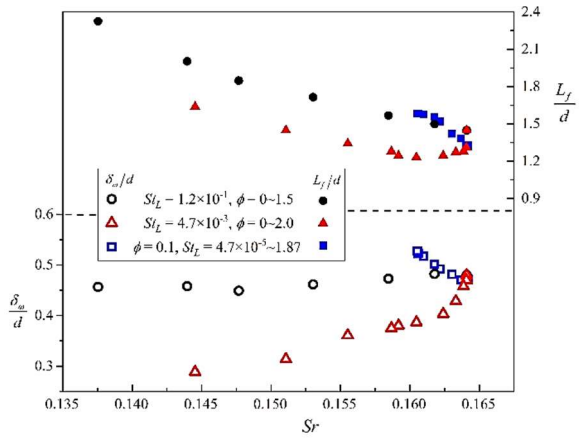

Fig. 20. Formation length and shear layer thickness as a function of Strouhal number.

this paper. It indicates that Strouhal number is a function of shear layer thickness and the formation length, i.e. $Sr = f(\delta_\omega, L_f)$. Specifically, Sr is negatively related with formation length L_f and overall positively related with shear layer thickness δ_ω.

Then, the Strouhal number physical equation for particle-laden wake flow would be developed based on the oscillating fishtail model, which is proposed for vortex shedding by Birkhoff (1953). As shown in Fig. 21, Birkhoff explained the Strouhal number considering the equilibrium between the hydraulic

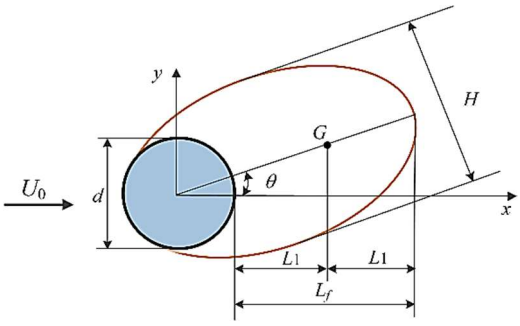

Fig. 21. Birkhoff 's oscillating fishtail model for vortex street wake flow (Birkhoff 1953).

restoring force acting on the dead stream behind the cylinder and the inertia force of the dead stream. The angular oscillation of a dead stream with the center of gravity at G about the axis of the cylinder is governed by

$$I\frac{d^2\theta}{dt^2}+k\theta=0 \tag{15}$$

where the moment of inertia of the dead stream $I=2\rho_f L_1 H(0.5d+L_1)$, the coefficient of restoring moment acting on the dead stream $k=2\pi\rho_f U_0^2 L_1(0.5d+L_1)$, H is the width of the dead stream, $2L_1$ is the length of the dead stream, θ is the inclination of the dead stream.

The natural frequency of the dead stream $f_{VS}=\omega_v/2\pi=U_0\big/\sqrt{4\pi H(0.5d+L_1)}$, and the Strouhal number is (Funakawa and Masaya 1969)

$$Sr=\frac{f_{VS}d}{U_0}=\frac{d}{\sqrt{4\pi H(0.5d+L_1)}} \tag{16}$$

Generally speaking, the length of the dead stream can be scaled by the length of formation region, i.e. $2L_1 = L_f$, and the dead stream width H is closely related with the cylinder diameter d (Funakawa and Masaya 1969). According to the study of Gerrard (1966) and the discussion in Section 4.2, the width of free shear layer diffuse (shear layer thickness) also affects the shedding frequency by influencing the vortex growing. Hence, in this study, we assume that $H = k_2 d + k_3\delta_\omega$, where k_2 and k_3 are constant coefficients. Then, the modified equation of Strouhal number is

$$Sr=\frac{1}{\sqrt{4\pi\left(k_2+k_3\frac{\delta_\omega}{d}\right)\left(\frac{1}{2}+\frac{1}{2}\frac{L_f}{d}\right)}} \tag{17}$$

Based on the law in Fig. 20 and the formula in Eq. (17), theoretically, the coefficient k_2 is positive and the coefficient k_3 is negative. In this study, $k_2 = 3.70$, $k_3 = -2.54$, which is consistent with the qualitative analysis. The predicted results by Eq. (17) is plotted in Fig. 22, where the percentage errors are within ± 1.5% error bands, the coefficient of determination R-square is 0.968, the relative root mean square error (rRMSE) is 0.78%, and the mean absolute percentage error (MAPE) is 0.67%. The fitting is satisfactory considering there will inevitably be some statistical errors during the data extraction for the characteristic lengths.

From the above analysis, it is concluded that the length of the formation region and the width of the free shear layers diffuse can be as the two characteristic lengths for the oscillating wakes. The proposed Strouhal number model in Eq. (17) gives a physical basis for the determination of the frequency characteristics by using these two characteristic lengths. The above discovers are beneficial for the further improvement of understanding on the dynamics of particle-vortex interactions.

5. CONCLUSION

The droplet-vortex interactions in vortex shedding was studied numerically by using the Euler-Lagrange approach. The numerical method was validated and a series of tests on different particle-laden conditions were conducted. The dynamics of droplet-vortex interactions were discussed by evaluating the particle dispersion in Karman vortex

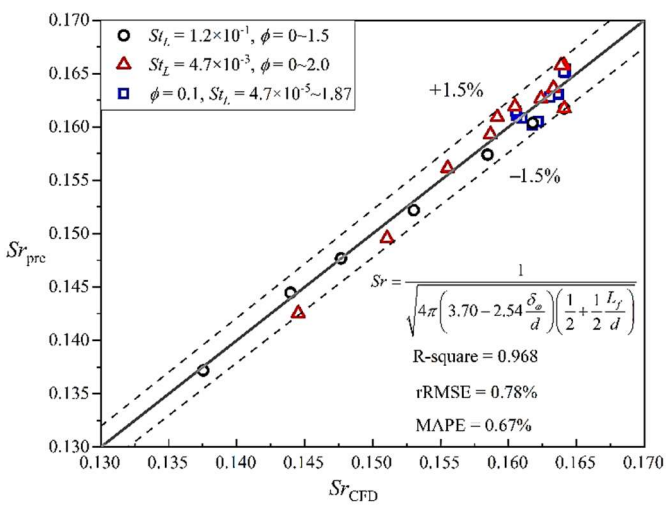

Fig. 22. Comparison between the actual and predicted Strouhal number by Eq. (17).

street and the frequency characteristics in particle-laden wake flow. Both the Eulerian and Lagrangian approaches were performed to quantify the particle dispersion. Two scaling parameters, Stokes number St_L and particle-fluid mass loading ratio ϕ were revealed, and the effect of St_L and ϕ on the dispersion and Strouhal number were analyzed from the particle response and the shear layer theory, respectively. The characteristic lengths of the wake flow were proposed to study the physical basis for the determination of the frequency. Finally, the Strouhal number physical model was developed based on the oscillating fishtail model. The main conclusions and findings are as follows:

1) The two independent scaling parameters, (i) the ratio of the particle's aerodynamic response time to the flow characteristic time, the Stokes number $St_L = \left(\rho_p/\rho_f\right) d_p^2 U_0 / 18\nu d$ and the particle-fluid mass loading ratio $\phi = m_p/m_f$, which constitute a dominant scaling group, can characterize both the particle dispersion dynamics and the wake vortex dynamics in Karman vortex street flows;

2) With the increase of Stokes number St_L, particle gradually separates from the vortex due to the centrifugal effect, three different regions can be observed, named instant following region ($St_L < 10^{-2}$), complete separation region ($St_L \geq 0.5$) and phase separation region ($10^{-2} \leqslant St_L < 0.5$); with the increase of mass loading ratio ϕ, the intensity and regularity of the shedding vortex get worse, which further disperses the droplet dispersion for their momentum exchange with irregular vortex structures;

3) The length of the formation region (formation length) and the width of the free shear layer diffuse (shear layer thickness) are the two simultaneous characteristic lengths for oscillating wakes of the particle-laden vortex street; the formation length is positively related with of St_L and ϕ on the whole, while the shear layer thickness is positively related with St_L and negatively related with ϕ;

4) Strouhal number is negatively related with formation length and overall positively related with shear layer thickness. The proposed modified Strouhal number model in Eq. (17) gives a physical basis for the determination of the frequency for particle-laden wake flows, the predicted errors are within $\pm 1.5\%$ error bands with mean absolute percentage error of 0.67%.

ACKNOWLEDGEMENTS

This work is supported by National Natural Science Foundation of China under Grant 51876143, 61873184 and 61627803, and the Fundamental Research Funds for the Central Universities of Civil Aviation University of China under Grant 3122021036.

REFERENCES

Aggarwal, S. K., T. W. Park and V. R. Katta (1996). Unsteady spray behavior in a heated jet shear-layer: droplet-vortex interactions. *Combustion Science & Technology* 113(1), 429−449.

Armenio, V. and V. Fiorotto (2001). The importance of the forces acting on particles in turbulent flows. *Physics of Fluids* 13(8), 2437–2440.

Birkhoff, G. (1953). Formation vortex street. *Journal of Applied Physics* 24(1), 98–103.

Bloor, M. S. (1964). The transition to turbulence in the wake of a circular cylinder. *Journal of Fluid Mechanics* 19(2), 290–304.

Bordás, R., V. John, E. Schmeyer and D. Thévenin (2013). Numerical methods for the simulation of a coalescence-driven droplet size distribution. *Theoretical & Computational Fluid Dynamics* 27(3−4), 253−271.

Burger, M., R. Schmehl, R. Koch, S. Witting and H. J. Bauer (2006). DNS of droplet–vortex interaction with a Karman vortex street. *International Journal of Heat & Fluid Flow* 27(2), 181−191.

Crowe, C. T., M. P. Sharma and D. E. Stock (1975). The particle-source-in cell (PSI-CELL) model for gas-droplet flow. *Journal of Fluids Engineering* 99(2), 325–332.

Crowe, C. T., R. A. Gore and T. R. Troutt (1985). Particle dispersion by coherent structures in free shear flows. *Particulate Science and Technology* 3(3-4), 149–158.

Crowe, C. T. (1991). The state-of-the-art in the development of numerical models for dispersed phase flows. In *Proceedings of International Conference on Multiphase Flows*, Tsukuba, Japan, 3, 49–60.

Dougherty, N., J. Holt, B. Liu and J. O' Farrell (2006). Time-accurate Navier-Stokes computations of unsteady flows - The Karman vortex street. In *Conference: 27th Aerospace Sciences Meeting*.

Eaton, J. K. and J. R. Fessler (1994). Preferential concentration of particles by turbulence. *International Journal of Multiphase Flow* 20(1), 169–209.

Fan, J., K. Luo, M. Y. Ha and K. Cen (2004). Direct numerical simulation of a near-field particle-laden plane turbulent jet. *Physical Review E* 70(2), 026303.

Fleckhaus, D., K. Hishida and M. Maeda (1987). Effect of laden solid particles on the turbulent flow structure of a round free jet. *Experiments in Fluids* 5(5), 323–333.

Funakawa, M. (1969). The Vibration of a Cylinder Caused by Wake Force in a Flow. *Bulletin of*

JSME 12(53), 1003–1010.

Gerrard, J. H. (1966). The mechanics of the formation region of vortices behind bluff bodies. *Journal of Fluid Mechanics* 25(2), 401.

Goldburg, A, W. K. Washburn and B. H. Florsheim (1965). Strouhal numbers for the hypersonic wakes of spheres and cones. *AIAA Journal* 3(7), 1332–1333.

Henderson, R. D. (1995). Details of the drag curve near the onset of vortex shedding. *Physics of Fluids* 7(9), 2102–2104.

Lazaro, B.J. and J.C. Lasheras (2006). Particle dispersion in the developing free shear-layer. I - Unforced flow. II - Forced flow. *Journal of Fluid Mechanics* 235, 179–221.

Li, J., C. Wang, H. Ding, Z. Zhang and H. Sun (2018). EMD and spectrum-centrobaric-correction-based analysis of vortex street characteristics in annular mist flow of wet gas. *IEEE Transactions on Instrumentation and Measurement* 37(5), 1150–1160.

Monkewitz, P. A. and L. N. Nguyen (1987). Absolute instability in the near-wake of two-dimensional bluff bodies. *Journal of Fluids & Structures* 1(2), 165–184.

Norberg, C. (1994). Experimental investigation of the flow around a circular cylinder: Influence of aspect ratio. *Journal of Fluid Mechanics* 258, 287–316.

Park, T. W., S. K. Aggarwal and V. R. Katta (1996). A numerical study of droplet-vortex interactions in an evaporating spray. *International Journal of Heat & Mass Transfer* 39(11), 2205−2219.

Park, J., K. Kwon and H. Choi (1998). Numerical solutions of flow past a circular cylinder at Reynolds numbers up to 160. *KSME International Journal* 12(6), 1200–1205.

Posdziech, O. and R. Grundmann (2007). A systematic approach to the numerical calculation of fundamental quantities of the two-dimensional flow over a circular cylinder. *Journal of Fluids & Structures* 23(3), 479–499.

Qiao, J., R. Deng and C. H. Wang (2015). Particle motion in a Taylor vortex. *International Journal of Multiphase Flow* 77, 120–130.

Qu, L., C. Norberg, L. Davidson, S. H. Peng and F. Wang (2013). Quantitative numerical analysis of flow past a circular cylinder at Reynolds number between 50 and 200. *Journal of Fluids & Structures* 39(5), 347–370.

Roshko, A. (1954). On the wake and drag of bluff bodies. *Journal of the Aeronautical Sciences* 22, 124–132.

Schmeyer, E., R. Bordás, D. Thévenin and V. John (2014). Numerical simulations and measurements of a droplet size distribution in a turbulent vortex street. *Meteorologische Zeitschrift* 23(4), 387−396.

Takahiko, B., H. Yosuke and T. Katsuroku (2009). Spontaneous motion of a droplet evolved by resonant oscillation of a vortex pair. *Physical Review E* 79(1), 031602.

Tang, L., C. T. Crowe, J. N. Chung and T. R. Troutt (1969). Effect of momentum coupling on the development of shear-layers in gas-particle mixtures. In *Proceedings of International Conference on the Mecnics of Two-phase Flows*, Taipei, Taiwan, 387–391.

Tomohiko, T. and J. K. Eaton (2008). Classification of turbulence modification by dispersed spheres using a novel dimensionless number. *Journal of Fluids Engineering* 101(11), 6037–6040.

Williamson, C. H. K. and A. Roshko (1990). A. Measurements of base pressure in the wake of a cylinder at low Reynolds numbers. *Zeitschrift fur Flugwissenschaften und Weltraumforschung* 14(1), 38–46.

Williamson, C. H. K. (1995). Vortex dynamics in the wake of a cylinder. In: *Green, S.I. (Ed.), Fluid Vortices*. Kluwer Academic Publishers, Amsterdam, Holland, 155–234.

Williamson, C. H. K. and G. L. Brown (1998). A series in $1/\sqrt{Re}$ to represent the Strouhal–Reynolds number relationship of the cylinder wake. *Journal of Fluids & Structures* 12(8), 1073–1085.

Yang, X., N. H. Thomas and L. J. Guo (2000). Particle dispersion in organized vortex structures within turbulent free shear flow. *Chemical Engineering Science* 55(7), 1305–1324.

Yang, Y., J. N. Chung, T. R. Troutt and C. T. Crowe (1993). The effects of particles on the stability of a two-phase wake flow. *International Journal of Multiphase Flow* 19(1), 137–149.